

Non-intrusive model reduction of advection-dominated hyperbolic problems using neural network shift augmented manifold transformations

Harshith Gowrachari^{*1}, Nicola Demo^{†1}, Giovanni Stabile^{‡2}, and Gianluigi Rozza^{§1}

¹Mathematics Area, mathLab, International School for Advanced Studies, via Bonomea 265, 34136 Trieste, Italy

²Biorobotics Institute, Sant'Anna School of Advanced Studies, V.le R. Piaggio 34, 56025, Pontedera, Pisa, Italy.

Abstract

Advection-dominated problems are commonly noticed in nature, engineering systems, and a wide range of industrial processes. For these problems, linear approximation methods (proper orthogonal decomposition and reduced basis method) are not suitable, as the Kolmogorov n -width decay is slow, leading to inefficient and inaccurate reduced order models. There are few non-linear approaches to accelerate the Kolmogorov n -width decay. In this work, we use a neural-network shift augmented transformation technique, that employs automatic-shift detection and detects the optimal non-linear transformation of the full-order model solution manifold \mathcal{M} . We exploit a deep-learning framework to derive parameter-dependent bijective mapping between the manifold \mathcal{M} and the transformed manifold $\tilde{\mathcal{M}}$. It consists of two neural networks, 1) ShiftNet, to employ automatic-shift detection by learning the shift-operator, which finds the optimal shifts for numerous snapshots of the full-order solution manifold, to accelerate the Kolmogorov n -width decay, and 2) InterpNet, which learns the reference configuration and can reconstruct the field values of the same, for each shifted grid distribution. We construct non-intrusive reduced order models on the resulting transformed linear subspaces and employ automatic-shift detection for predictions. We test our methodology on advection-dominated problems, such as 1D travelling waves, 2D isentropic convective vortex and 2D two-phase flow test cases. This work leads to the development of the complete NNsPOD-ROM algorithm for model reduction of advection-dominated problems, comprising both offline-online stages.

1 Introduction

Industries have a keen interest in obtaining reduced-order models (ROMs) for engineering systems, especially for control, optimization, and uncertainty quantification problems. ROMs offer computational efficiency for many-query scenarios and are suitable for real-time computations. These models simplify the high-dimensional parametric partial differential equations (PDEs) by creating low-rank approximations, significantly reducing the computational cost of numerical simulations compared to the full-order models (FOMs).

To solve the parametric PDEs that describe real-world scenarios, various numerical methods are used, such as the finite element method (FEM), the finite volume method (FVM), the discontinuous Galerkin method (DGM), and the spectral element method (SEM). While these methods are accurate, they are also computationally intensive. The ROM framework addresses this by dividing the process into two stages:

- Offline (training) stage: This expensive phase involves computing a set of FOM solutions (snapshots) and constructing the ROM based on a low-dimensional approximation subspace of the FOM solution manifold.
- Online (testing and predictive) stage: This cost-efficient phase uses the compressed information from the offline stage to predict reduced solutions for new, unseen parameters, significantly reducing the computation costs.

*hgowrach@sissa.it

†ndemo@sissa.it

‡giovanni.stabile@santannapisa.it

§grozza@sissa.it

There are various model reduction methods [35, 16, 5, 39] to obtain low-rank approximation of the FOM solution manifold, in that proper orthogonal decomposition (POD) and reduced basis (RB) methods are the most popular and promising techniques for various fluid dynamics and solid mechanics applications [39]. The main assumption considered in these methods is, that the solution of a parameterized PDEs exists on the low-dimensional manifold, which can be approximated by a linear combination of a few global basis functions, obtained from the solutions of the FOM. The low-dimensional manifold/subspace of the high-dimensional FOM solution manifold can be obtained by both linear and non-linear trial subspaces. In linear subspaces methods, there are POD and RB method using greedy approach, and the non-linear trial subspaces can be obtained by several machine learning techniques. In reduce order modeling, once the low-dimensional approximation subspace of the FOM solution manifold is obtained, to compute the evolution of the dynamics in the low-dimensional manifold, modal coefficients or latent coordinates need to be computed and for this, there are intrusive and non-intrusive approaches. In the intrusive approach, the discretized PDEs (governing equations) are projected onto a low-dimensional subspace to obtain a system of low-dimensional ODEs, this procedure of ROM construction is known as Galerkin or Petrov-Galerkin projection-based ROM [42, 43]. As this approach leverages equations, it is inherently physics-based and usually demonstrates better extrapolation properties. However, this method requires knowledge of the underlying equations and access to the discretized differential operators constructed by the full-order model, meaning complete access to the internal data structure of the solver, which makes it quite prohibitive for the application in industrial settings. For the case of non-linear/non-affine problems, the intrusive approach does not yield significant speed-up. Conversely, the non-intrusive approaches, that are purely data-driven (with no equations requirement), ensure the significant speed-up even for non-linear/non-affine problems. In this work we focus exclusively on non-intrusive approaches, once the set of snapshots is computed, the ROM is constructed using POD with interpolation (POD-I). The original snapshot set is projected onto POD modes to obtain modal coefficients, interpolation or regression is used to evaluate modal coefficients for new unseen parameters and various techniques can be employed for interpolation task, which is discussed later in subsection 2.2.

For advection-dominated problems, e.g., convection-dominated flows, travelling waves and shock propagation, it is difficult to find the low-dimensional linear approximation subspace for the development of accurate and efficient ROM, as solution manifolds of these problems exhibit slow Kolmogorov n -width (KnW) decay. The KnW provides a rigorous measure of the reducibility of the solution manifold by linear approximation/compression methods, such as POD and RB method using greedy approaches. For the solution manifold \mathcal{M} consisting of f elements, embedded in some normed linear space $(X_{\mathcal{N}}, \|\cdot\|_{X_{\mathcal{N}}})$, the definition of Kolmogorov n -width $d_n(\mathcal{M})$ is as follows:

$$d_n(\mathcal{M}) := \inf_{E_n \subset X_{\mathcal{N}}} \sup_{f \in \mathcal{M}_N} \inf_{g \in E_n} \|f - g\|_{X_{\mathcal{N}}}, \quad (1)$$

where E_n is linear subspace of $X_{\mathcal{N}}$ of dimension n . The Kolmogorov n -width $d_n(\mathcal{M})$ represents the worst error we commit by approximating any element f of \mathcal{M} with approximated element g of a linear subspace E_n of dimension n . Moreover, the faster the KnW $d_n(\mathcal{M})$ decreases with increasing n , the low-dimensional linear approximation subspace of dimension n becomes more effective at approximating the solution manifold \mathcal{M} . Even the solution manifold of a simple linear advection problem exhibits slow KnW decay [33] and the use of linear approximation methods leads to the construction of inefficient linear ROMs.

Advection-dominated problems are characterized by high-dimensional features, resulting in a slow KnW decay of the FOM solution manifold. This means there is no low-dimensional linear approximation subspace that can effectively approximate FOM solutions. Consequently, linear model reduction methods such as POD and RB are unsuitable, leading to inefficient and inaccurate linear-projection-based ROMs for these problems. In recent years there has been significant development in model-reduction methods to overcome the barrier of this slow KnW decay, which are leading towards non-linear approaches [33], particularly by performing model-reduction on non-linear manifolds, by obtaining non-linear trial subspaces using convolutional auto-encoders (CAEs) [20, 15, 6, 17, 24, 11, 21, 38] and using quadratic approximation manifold [19, 1, 12]; by incorporating adaptive local-in-parameter and/or local-in-space enrichment strategies [14, 48, 34, 32, 2]; and by transforming the linear subspace by employing transport maps using registration methods [29, 26, 18, 27, 4, 37, 45, 46, 28]. Further, these non-linear approaches can be divided into Eulerian and Lagrangian approaches [45]. Among those of Eulerian approaches, there are few recent transformation techniques [45, 30, 25] that can be exploited for non-linear transformations

of the full-order solution manifold. This leads to a transformed manifold with accelerated KnW decay, resulting in low-dimensional transformed linear approximation subspace and enabling the construction of accurate and efficient reduced order models.

In our work, we use the neural-network shift-augmented nonlinear transformation technique introduced in the neural-network shifted-proper orthogonal decomposition (NNsPOD) framework [30]. The NNsPOD method incorporates automatic shift detection, independent of the underlying equation and overcomes the limitations of the shifted-POD approach [36], which requires a-priori the complete knowledge (i.e., advection velocity) of the problem in hand. The neural-network shift-augmented nonlinear transformation technique seeks for optimal mapping of numerous snapshots to reference frame, to obtain low-dimensional transformed linear approximation subspace by employing neural-networks for automatic-shift detection. This approach does not require a-priori the complete knowledge (e.g., advection velocity, underlying governing equation) of the problem in hand. The previous work of NNsPOD mainly focuses on the model reduction of FOM non-linear solution manifolds governed by hyperbolic PDEs. It solely reports non-linear transformation of solution manifold using neural-network shift-augmented transformation and followed by POD (hence, the name NNsPOD), to obtain transformed linear subspace with accelerated KnW decay. It only covers part of the offline stage of the ROM framework, just the model reduction using NNsPOD and the complete algorithm comprising of offline and online stages is not reported.

In this work, we extend the applicability of the NNsPOD framework, by proposing a complete algorithm comprising offline-online stages, for the construction of efficient ROMs using NNsPOD, and we test our proposed methodology by applying to 1D travelling waves and challenging 2D test cases, both the advection-dominated problems are governed by hyperbolic PDEs. The main contribution of our work is as follows: 1) construction of reduced order model on the transformed linear subspace, obtained by performing model reduction using NNsPOD, 2) employment of automatic shift detection in the online stage (predictive and testing phase) and 3) the complete NNsPOD-ROM algorithm comprising of both offline and online stages, for the construction of accurate and efficient ROMs is reported. We came across that the works reported in [22, 3] propose a workflow for the development of ROM using shifted-POD comprising of offline-online stages, in which neural networks are employed for mapping parameters to modal coefficients and also for the mapping of shifts, particularly for the predictions in the online stage. But, in our work we use neural-networks for the automatic-shift detection, to transport/map all the snapshots to the reference frame, resulting in the transformation of linear subspace and yielding the low-dimensional linear approximation subspace at the reference frame, for the construction of efficient ROMs. Then we employ this automatic-shift detection, for predictions in the online stage.

This paper is organised as follows, we introduce the methodology in section 2, in which we discuss the neural-network shift augmented transformation approach in subsection 2.1 and the construction of non-intrusive or data-driven reduced order model by performing linear dimensionality reduction and the solution manifold approximation in subsection 2.2; in section 3 we discuss the implementation of the complete algorithm for the development of NNsPOD based ROM comprising of both offline-online stages; in section 4 we test our methodology by applying to advection-dominated problems governed by hyperbolic PDEs, by first applying to 1D travelling wave toy problem to illustrate the complete workflow of the algorithm, then applied to 2D isentropic convective vortex and 2D two-phase flow test cases; and finally the conclusions, perspectives and future directions are discussed in section 5.

2 Methodology

In this section, we discuss the employment of automatic-shift detection by exploiting deep learning architectures, specifically, the Artificial Neural Networks (ANNs) to transform the FOM solution manifold, aiming to accelerate the KnW decay, ensuring the existence of low-dimensional linear approximation subspace, and discussing the construction of the efficient and accurate non-intrusive reduced order model [39] using the transformed linear subspace.

2.1 Neural-Network shift augmented transformation

The preliminary idea behind the neural network shift augmented transformation of solution manifold is derived from shifted-POD (sPOD) [36]. In sPOD approach, snapshots are translated in space to reference frame/configuration using a shifting operator $\mathcal{T}_{\mathbf{b}}$, that acts on the field $\mathbf{u}(\mathbf{x}, t; \boldsymbol{\mu})$ as in (2), where $\tilde{\mathbf{u}}(\mathbf{x}, t; \boldsymbol{\mu})$

is the shifted field defined in spatial domain $\Omega \subset \mathbb{R}^d$, $d = \{1, 2, 3\}$, with varying time t in interval $[0, T_{\boldsymbol{\mu}}]$ and parameter space $\boldsymbol{\mu} \in \mathcal{P} \subset \mathbb{R}^p$, and with the advection velocity \mathbf{b} . Here, the shifting quantity is a fixed value linearly depending on time. The application of shifted-POD (sPOD) [36] depends on the complete knowledge of the advection velocities of a given problem, being the main drawback of this approach.

$$\tilde{\mathbf{u}}(\mathbf{x}, t; \boldsymbol{\mu}) = \mathcal{T}_{\mathbf{b}}\mathbf{u}(\mathbf{x}, t; \boldsymbol{\mu}) = \mathbf{u}(\mathbf{x} - \mathbf{b}t, t; \boldsymbol{\mu}), \quad (\mathbf{x}, t, \mathbf{b}) \in \Omega_{\boldsymbol{\mu}} \times [0, T_{\boldsymbol{\mu}}]. \quad (2)$$

The NNsPOD approach [30, 39] overcomes the drawback of sPOD, by employing a semi-supervised learning paradigm for automatic-shift detection, meaning it automatically finds the optimal shifts for numerous snapshots to the reference configuration, and here, the reference snapshot is chosen from one among the snapshot set. The NNsPOD approach [30], introduces neural-network shift augmented manifold transformation and is followed by linear compression POD, for non-linear reduction of hyperbolic equations. In this approach, the deep-learning framework is exploited to derive bijective transformations/mapping between the original manifold \mathcal{M} and the shifted-manifold $\tilde{\mathcal{M}}$ as shown in (3). It does not require any prior knowledge of the physical properties of the given problem and no knowledge of underlying equations (physical models) is required, overcoming the limitation of sPOD. Here, we learn the shift operator $\mathcal{T}_{\text{shift}}$ using neural-networks, which acts on the field $\mathbf{u}(\mathbf{x}, t; \boldsymbol{\mu})$ as in (4), where $\mathcal{T}_{\text{shift}} : \Omega_{\boldsymbol{\mu}} \times [0, T_{\boldsymbol{\mu}}] \rightarrow \Omega$, is the shifting quantity that is not a fixed value linearly depending on time as in (2), but it depends on both, the space and time in this approach.

$$\mathcal{C}^1 \ni \mathcal{T}_{\mathbf{b}} : \mathcal{M} \mapsto \tilde{\mathcal{M}}, \quad (3)$$

$$\mathcal{T}_{\mathbf{b}} : \mathcal{M} \mapsto \tilde{\mathcal{M}}, \quad \tilde{\mathcal{M}} := \{\mathbf{u}(\mathbf{x} - \mathcal{T}_{\text{shift}}(\mathbf{x}, t), t; \boldsymbol{\mu}) \mid (\mathbf{x}, t) \in \Omega_{\boldsymbol{\mu}} \times [0, T_{\boldsymbol{\mu}}]\}. \quad (4)$$

Here, we use ANNs to learn this shift operator for a given problem, in principle one can opt to use different architectures depending on the complexity of the problems. The learning process is built on the set of snapshots as a discrete field, as defined in (5), where \mathbb{V} is the discretized domain, and t_i are the N_s time steps. The key idea is to transform these snapshots by minimizing the Euclidean distance between them and a chosen reference configuration, \mathbf{u}_{ref} , and the loss function $\mathcal{L}_{\text{ShiftNet}}$ employed for this process is shown in (7). After the shift-detection, another important step in this transformation technique is the reconstruction of the field values in each shifted-space. Conventionally, interpolation is used for the reconstruction of field values. But, here we employ a neural network for reconstructing field values, it will learn the reconstruction of the reference configuration field values, and the loss function $\mathcal{L}_{\text{InterpNet}}$ considered for this is the mean squared error (MSE) function as in (6), where n is the number of cells or grid points.

$$\{\mathbb{V} \ni \mathbf{u}(t_i; \boldsymbol{\mu})\}_{i=1}^{N_s} = \{u(\mathbb{V}, t_i; \boldsymbol{\mu})\}_{i=1}^{N_s}, \quad (5)$$

$$\mathcal{L}_{\text{InterpNet}} = \frac{1}{n} \sum_{j=1}^n \|\mathbf{x}_j - \mathbf{u}_{\text{ref}}(\mathbf{x}_j, t; \boldsymbol{\mu})\|_2, \quad \mathbf{x} \in \mathbb{V}, \quad (6)$$

$$\mathcal{L}_{\text{ShiftNet}} = \frac{1}{N_s} \sum_{i=1}^{N_s} \|\mathbf{u}_{\text{ref}}(\mathbf{x}, t_i; \boldsymbol{\mu}) - \mathbf{u}(\mathbf{x} - \mathcal{T}_{\text{shift}}(\mathbf{x}, t_i), t_i; \boldsymbol{\mu})\|_2, \quad \mathbf{x} \in \mathbb{V}. \quad (7)$$

In this transformation technique, the automatic-shift detection and the reconstruction of field values workloads are divided between two separate neural networks :

- **ShiftNet** will learn the shift operator for a given problem, which quantifies the optimal-shift $\mathcal{T}(x, t)$, resulting in shifted space that transports all the snapshots to the reference frame.
- **InterpNet** will learn the reference configuration w.r.t its grid distribution and reconstruct the reference configuration shape/field values for each shifted space, to compute the distance. It is mainly employed to function as an interpolator, to obtain field values in each shifted space.

2.2 Reduced Order Modelling

In this section, we discuss the construction of ROM using proper orthogonal decomposition (POD), a widely used linear dimensionality reduction method to compress the solution manifold and a promising method in the ROM community in the last few decades, particularly with applications in CFD.

2.2.1 Proper Orthogonal Decomposition

After the neural-network shift augmented transformations, we obtain the low-rank approximation of the transformed snapshot matrix \mathcal{X} , by performing linear dimensionality reduction using POD. The transformed snapshot matrix consists of column-wise entries of neural network shift augmented snapshots $\tilde{\mathbf{u}}_i$ of n corresponding parameters $\boldsymbol{\mu}$. The transformed snapshots $\tilde{\mathbf{u}}_i(\mathbf{x}, t; \boldsymbol{\mu})$ can be expressed by a linear combination of global basis functions as shown in (8), approximating the transformed snapshots by few global basis functions (modes) $\varphi_k \in \mathbb{R}^n$ and few modal coefficients $c_i^k \in \mathbb{R}$. The linear approximation space $\mathcal{V}_n = \{\varphi_1, \dots, \varphi_n\}$ is fixed and independent of the $\tilde{\mathbf{u}}_i(\mathbf{x}, t; \boldsymbol{\mu})$ to be approximated. We obtain transformed linear subspace by decomposing transformed snapshot matrix \mathcal{X} by performing POD using Singular value decomposition (SVD) [44] as in (9),

$$\tilde{\mathbf{u}}_i = \sum_{k=1}^n \varphi_k c_i^k \approx \sum_{k=1}^r \varphi_k c_i^k \quad \forall i \in [1, \dots, n], \quad r \ll n, \quad (8)$$

$$\underbrace{\mathcal{X}}_{m \times n} = \underbrace{\mathbf{U}}_{m \times m} \underbrace{\boldsymbol{\Sigma}}_{m \times n} \underbrace{\mathbf{V}^T}_{n \times n} \Rightarrow \underbrace{\mathcal{X}}_{m \times n} \approx \underbrace{\hat{\mathbf{U}}}_{m \times r} \underbrace{\hat{\boldsymbol{\Sigma}}}_{r \times r} \underbrace{\hat{\mathbf{V}}^T}_{r \times n}, \quad (9)$$

where, \mathbf{U} and \mathbf{V} are the two orthonormal matrices and hence, unitary matrices, $\mathbf{U}^T \mathbf{U} = \mathbf{V}^T \mathbf{V} = \mathbb{I}$, where \mathbb{I} is identity matrix. Columns of \mathbf{U} are the left singular vectors, also called POD modes and columns of \mathbf{V} are right singular vectors of the transformed snapshot matrix \mathcal{X} respectively. $\boldsymbol{\Sigma}$ is the diagonal matrix with n real singular values, arranged in descending order $\sigma_1 > \sigma_2 > \sigma_3 \dots \sigma_{\min(m,n)} > 0$, which indicates the energy contribution of the corresponding modes. As stated in Schmidt–Eckart–Young–Mirsky theorem [10], our interest is to seek for low-dimensional subspace that approximates to \mathcal{X} , is obtained by choosing the first r number of singular values and their corresponding left singular vectors or POD modes. The r singular values are chosen based on the user-provided tolerance k , the ratio of the energy contained by the first r modes and the energy contained by all n modes as shown in (10), indicating the percentage of energy retained by first r modes.

$$\frac{\sum_{i=1}^r \sigma_i^2}{\sum_{i=1}^n \sigma_i^2} = \kappa. \quad (10)$$

Once we have the r POD modes, we compute coefficient matrix C as shown in (11) consisting of the modal coefficients, by projecting the transformed snapshot matrix onto the POD modes. We can only reconstruct the transformed snapshot set using these coefficients by following the procedure (8). To predict accurate snapshots for new unseen parameters, we have to construct parameters to modal coefficients map, discussed in the next subsection. Then, just by simple matrix multiplication, we can obtain the transformed snapshots of interest.

$$C = U^T \mathcal{X}. \quad (11)$$

2.2.2 Solution Manifold Approximation

There are several choices available for solution manifold reconstruction described by the modal coefficients corresponding to the initial database, in our case the transformed snapshots matrix. Here, the main aim is to construct a regression $s : \mathcal{P} \mapsto \mathbb{R}^r$ which approximates the map f as in (12) given by a set of m input-output pairs $\{\mu_i, c_i\}_{i=1}^m$, where μ_i is the parameter value associated with the i^{th} snapshot and c_i are the corresponding POD coefficients obtained by (11).

$$f : \mu \in \mathcal{P} \mapsto c \in \mathbb{R}^r. \quad (12)$$

Then this constructed regression model is used to predict the snapshot \mathbf{u}^* for a new unseen input parameter μ^* by computing,

$$\mathbf{u}^* = U s(\mu^*). \quad (13)$$

To device this regression s for the parameters to coefficients mapping, there are several techniques namely linear interpolation, non-linear Gaussian process regression (GPR), radial basis function (RBF) interpolation, multi-fidelity methods, inverse distance weighting (IDW) and artificial neural networks (ANNs), to name few. In this work, we mainly use radial basis function (RBF) interpolation to build parameters to modal coefficients map.

3 NNsPOD-ROM algorithm

In this section, we discuss the complete workflow for developing ROM using NNsPOD. The workflow can be divided into two stages as reported in Algorithm 1, FOM pre-processing (offline stage), which comprises of NNsPOD and constructing ROM and FOM post-processing (online stage), for testing and prediction of snapshots for given parameters.

For the given input, parameters and their corresponding snapshots, reference configuration index, neural-networks architecture and respective stopping criterion, the training of InterpNet and ShiftNet is separated and at first, InterpNet is trained and later the ShiftNet. The InterpNet should be able to learn and reconstruct the field value of the reference configuration, whose forward map will used to reconstruct field values during ShiftNet training and for this reason the InterpNet loss function $\mathcal{L}_{\text{InterpNet}}$ must be optimised and is of keen importance. During ShiftNet training, for each shifted space, $\tilde{\mathbf{x}}_i^{\text{shift}}$, the field values are obtained using trained InterpNet forward map and the ShiftNet loss function $\mathcal{L}_{\text{ShiftNet}}$ is minimized to learn the optimal shift operator.

After the completion of training (reaching the desired criterion), for each input parameter, we obtain the optimal shifted space $\tilde{\mathbf{x}}_i^{\text{ref}}$ that shifts/transport the snapshot to reference frame, by backward mapping (subtracting) the reference configuration grid distribution by optimal shift (obtained by ShiftNet forward map). Once we have the shifted space $\tilde{\mathbf{x}}_i^{\text{ref}}$, which transports the snapshots field values to reference frame, we need to reconstruct these snapshots field values w.r.t the reference configuration grid distribution \mathbf{x}_{ref} or physical space \mathbf{x} ($\mathbf{x}_{\text{ref}} = \mathbf{x}$), for which we use linear interpolator. After this step, all the snapshots are at the reference frame and in the same grid distribution, now we perform reduction to achieve sharp KnW decay and get low-dimensional transformed linear approximation subspace, obtaining r number of POD modes to construct ROM, by the following the steps mentioned the previous subsection 2.2.

In FOM post-processing (online stage), the predicted snapshots are at the reference frame, to shift back or transport the snapshot to the correct frame for a given parameter, the shifts are forward mapped (added) to reference grid distribution, to obtain $\tilde{\mathbf{x}}$. Once we have the shifted space $\tilde{\mathbf{x}}$ that transports the predicted snapshots to the correct frame, again we have to reconstruct the field values of the predicted snapshots in physical space, for which we use linear interpolator in this step. Now, the predicted snapshots are in physical space and the field values intensity variations are at the correct frame/location.

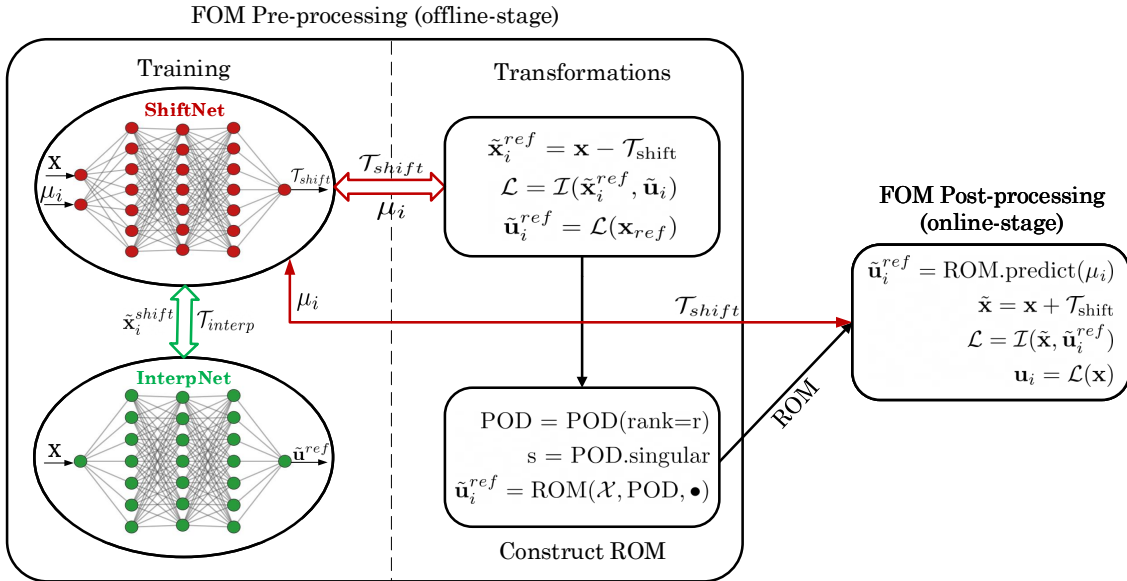


Figure 1: Schematic representation of the complete workflow for the development of NNsPOD-ROM. The offline stage consists of training of neural-networks, transformations and construction of ROM, and in the online stage, the automatic-shift detection is employed for the predictions.

Algorithm 1: NNsPOD-ROM

Data: Input parameters $\mu_i \in \mathcal{P}$ and corresponding snapshots $\mathbf{u}_i \in \mathbf{X}$, where $i = 0, \dots, N_{\text{train}}$; r number of POD modes; reference configuration index; InterpNet and ShiftNet architecture and respective criterion $\epsilon_{\text{interp}}, \epsilon_{\text{shift}}$ for loss functions.

Result: NNsPOD-ROM prediction of snapshots for given parameter μ_i

FOM pre-processing : offline stage

```

while  $\mathcal{L}_{\text{InterpNet}} > \epsilon_{\text{interp}}$  do
  InterpNet.forward ;
  compute  $\mathcal{L}_{\text{InterpNet}}$  ;
  InterpNet.backward ;
end
 $\mathcal{T}_{\text{interp}} = \text{InterpNet.forward}$ ;          # reconstruct field values of reference snapshot
for  $\mu_i \in \mathcal{P}, \mathbf{u}_i \in \mathbf{X}$ , where  $i = 0$  to  $N_{\text{train}}$  do
  while  $\mathcal{L}_{\text{ShiftNet}} > \epsilon_{\text{shift}}$  do
     $\mathbf{x}_i^{\text{shift}} = \mathbf{x}_i - \text{ShiftNet.forward}$ ;          # x is physical space (x =  $\mathbf{x}_{\text{ref}}$ )
     $\tilde{\mathbf{u}}_i = \mathcal{T}_{\text{interp}}(\mathbf{x}_i^{\text{shift}})$ ;          # reconstruct snapshot at each shifted space
    compute  $\mathcal{L}_{\text{ShiftNet}}$  ;
    ShiftNet.backward ;
  end
   $\mathcal{T}_{\text{shift}} = \text{ShiftNet.forward}$ ;          # optimal shift for given parameter
   $\tilde{\mathbf{x}}_i^{\text{ref}} = \mathbf{x} - \mathcal{T}_{\text{shift}}$ ;          # shifted space that transports to reference frame
   $\mathcal{L} = \mathcal{I}(\tilde{\mathbf{x}}_i^{\text{ref}}, \tilde{\mathbf{u}}_i)$ ;          # interpolator
   $\tilde{\mathbf{u}}_i^{\text{ref}} = \mathcal{L}(\mathbf{x}_{\text{ref}})$ ;          # reconstructed snapshots are at reference frame
end
POD = POD(rank=r);          # POD object, returns r modes
s = POD.singular_values ;          # get Singular values with fast decay
 $\tilde{\mathbf{u}}_i^{\text{ref}} = \text{ROM}(\mathcal{X}, \text{POD}, \bullet)$ ;          # construct ROM,  $\bullet = \text{Linear, GPR, RBF or ANN}$ 

```

FOM post-processing : online stage

```

for  $\mu_i \in \mathcal{P}$ , where  $i = 0$  to  $N_{\text{test}}$  do
   $\tilde{\mathbf{u}}_i^{\text{ref}} = \text{ROM.predict}(\mu_i)$ ;          # predictions at reference frame
   $\tilde{\mathbf{x}} = \mathbf{x} + \mathcal{T}_{\text{shift}}$ ;          # shifted back to correct frame
   $\mathcal{L} = \mathcal{I}(\tilde{\mathbf{x}}, \tilde{\mathbf{u}}_i^{\text{ref}})$ ;          # interpolator
   $\tilde{\mathbf{u}}_i = \mathcal{L}(\mathbf{x})$ ;          # predicted snapshots for test parameters
end
Get  $\tilde{\mathbf{u}}_i$  in physical space,  $\mathbf{x}$ , and compute relative  $L_2$ -norm error ;
 $\tilde{\mathbf{u}}_{\text{new}} = \text{ROM.predict}(\mu_{\text{new}})$ ;          # predictions for unseen new parameters

```

To address the accuracy of the predictions, we compute the relative L_2 error of the predicted snapshots $\tilde{\mathbf{u}}$, which is defined as in (14). Where \mathbf{u}_i is the original or true field value and $\tilde{\mathbf{u}}_i$ is the ROM predicted field value at i^{th} cell,

$$\mathcal{L}_2 = \frac{\|\mathbf{u} - \tilde{\mathbf{u}}\|}{\|\mathbf{u}\|} = \frac{\sqrt{\sum_{i=0}^n (\mathbf{u}_i - \tilde{\mathbf{u}}_i)^2}}{\sqrt{\sum_{i=0}^n (\mathbf{u}_i^2)}}. \quad (14)$$

The implementation of this Algorithm 1 is carried out using EZyRB package [8], which is a python library of data-driven model-order-reduction for parameterized problems and here, the implementation of Deep Neural Networks is carried out using PyTorch package [31]. The schematic representation of the complete workflow of the NNsPOD-based ROM algorithm is shown in Figure 1.

4 Numerical Experiments

In this section, we test our methodology by demonstrating the application of NNsPOD to develop ROMs for advection-dominated problems. Here, we consider three test cases, 1D Travelling Waves, 2D Isentropic Convective Vortex and 2D Two-phase flow.

4.1 1D Travelling Waves

We consider a parameterized 1D Gaussian function (15) to mimic 1D soliton waves, in which constant $\alpha = 1$, $x \in [0, 10.25]$ is spacial coordinate, t is mean and σ^2 is variance, where σ is the standard deviation. Here, σ is kept constant, we parameterize the mean $t \in [0, 10.25]$, where changing t shifts the distribution and for our convenience we consider the mean t parameter as time, to treat this as a parameterized time-dependent problem. The main reason to consider this test case is to illustrate the complete workflow of the algorithm. We generate a database consisting of 20 parameters and their corresponding snapshots w.r.t to 256 equidistant nodes $x \in [0, 10.25]$, as shown in Figure 2, from which we divide 50% of the database as training set (Figure 4, Left) and the rest as testing set.

$$f(t) = \alpha e^{-(x-t)^2/(2\sigma^2)}. \quad (15)$$

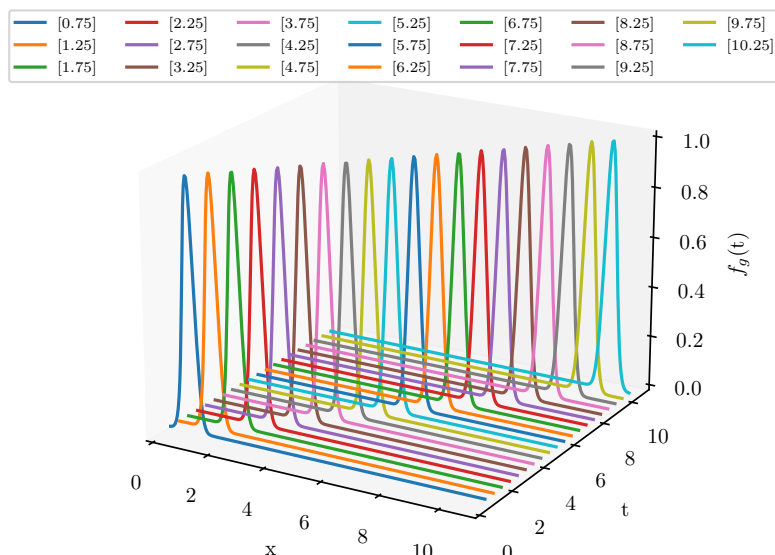


Figure 2: 1D travelling waves original snapshots corresponding to 20 parameters, $t \in [0, 10.25]$, in physical space $x \in [0, 10.25]$, divided into 256 equidistant nodes.

For the training of neural-network shift augmented transformations, the snapshot of the reference parameter 3.25 from the training set, is considered as reference configuration. The settings considered for the two neural network architectures for this test case are as shown in Table 2. InterpNet learns to reconstruct the field values of the reference snapshot as shown in Figure 3 (left). This is used by ShiftNet to find the optimal shift in physical space, such that the snapshots in their respective shifted space are translated to reference frame/configuration, as shown in the Figure 3 (right) for the parameter $\mu = 6$. These shifted/transported snapshots to reference frame in their respective shifted space, are reconstructed in physical space using interpolation as shown in the Figure 3 (right) labelled as Shifted.

After the shift augmented transformations of the FOM solution manifold (training set), all the snapshots of the training set are transported to the reference frame as shown in Figure 4. Then, we seek the low-dimensional linear approximation subspace by performing reduction on this transformed manifold \mathcal{X} using Singular Value Decomposition (SVD), by obtaining sharp KnW decay. The resulting sharp singular values decay and the first most energetic POD mode is shown in Figure 5. The modal coefficients are obtained by projecting the training set data \mathcal{X} onto the POD space, and these modal coefficients can only be used to reconstruct the original snapshots. To obtain a fast and accurate prediction of snapshots

for given unseen parameters, we build parameters to modal coefficients map using Radial Basis Functions (RBF). Then, by simple matrix multiplication, we obtain the snapshot of any parameter of interest. The predicted snapshots for test set parameters, compared with their respective analytical solution are shown in Figure 6. The reconstruction error for both train and test set parameters is shown in Figure 7 and the error variation in the same order of magnitude can be depicted, meaning the resulted ROM predicts reliable accurate snapshots for the new unseen parameter.

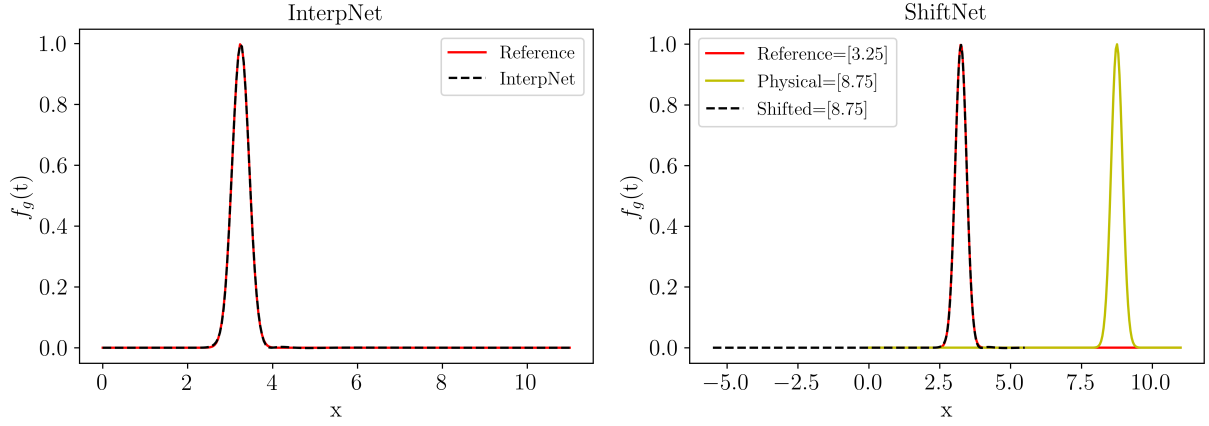


Figure 3: For 1D Travelling waves, **Left**: Showing trained InterpNet, able to reconstruct the field values of reference snapshot and **Right**: The original snapshot for parameter $t = 6$ (labelled as physical), transported to the reference frame in shifted space (labelled as shifted), by using optimal shift obtained by trained ShiftNet forward map, along that with showing the reference snapshot (frame).

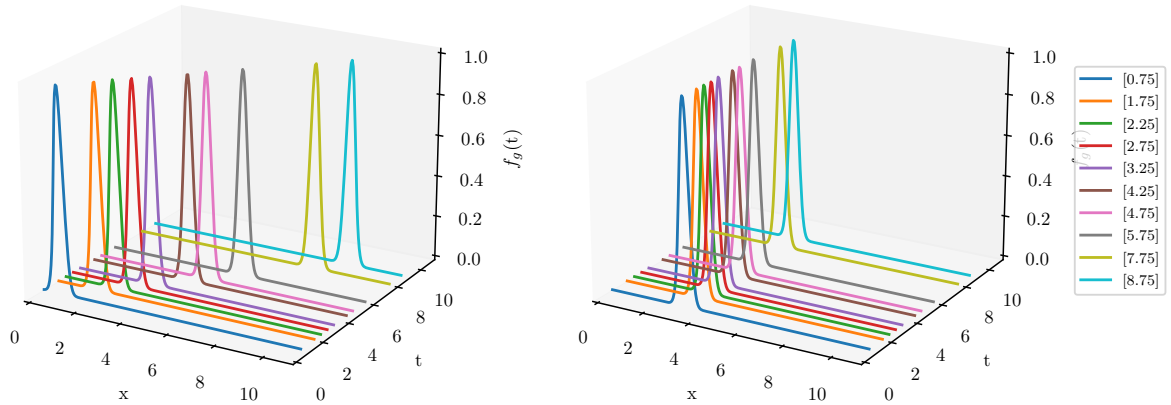


Figure 4: **Left**: 1D Travelling waves training set original snapshots in physical space and **Right**: the same snapshots shifted to the reference frame (right side) in physical space after neural-network shift augmented transformations.

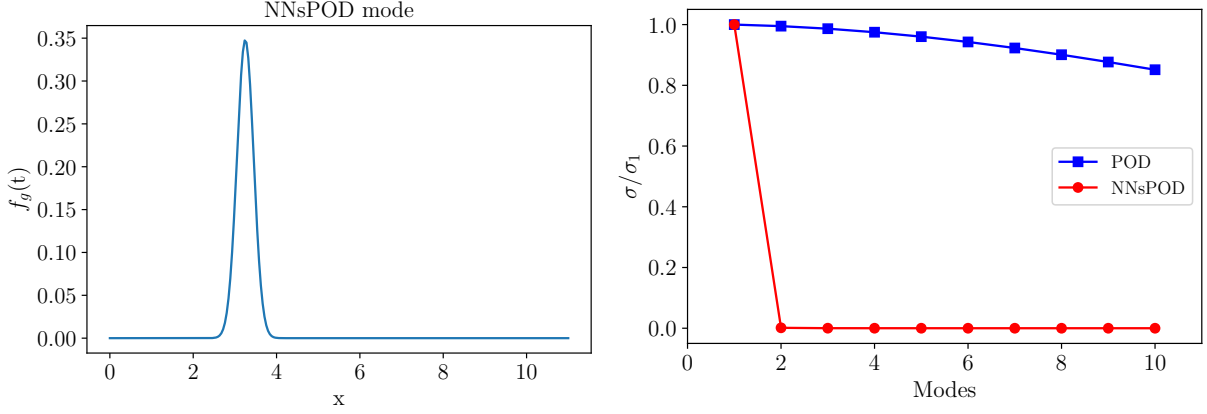


Figure 5: **Left:** 1D Travelling wave first POD mode, obtained after the neural-network shift augmented manifold transformation and **Right:** Comparison of singular values decay of 1D Travelling wave FOM manifold without pre-processing, labelled as POD and after the neural-network shifted augmented manifold transformation, labelled as NNsPOD.

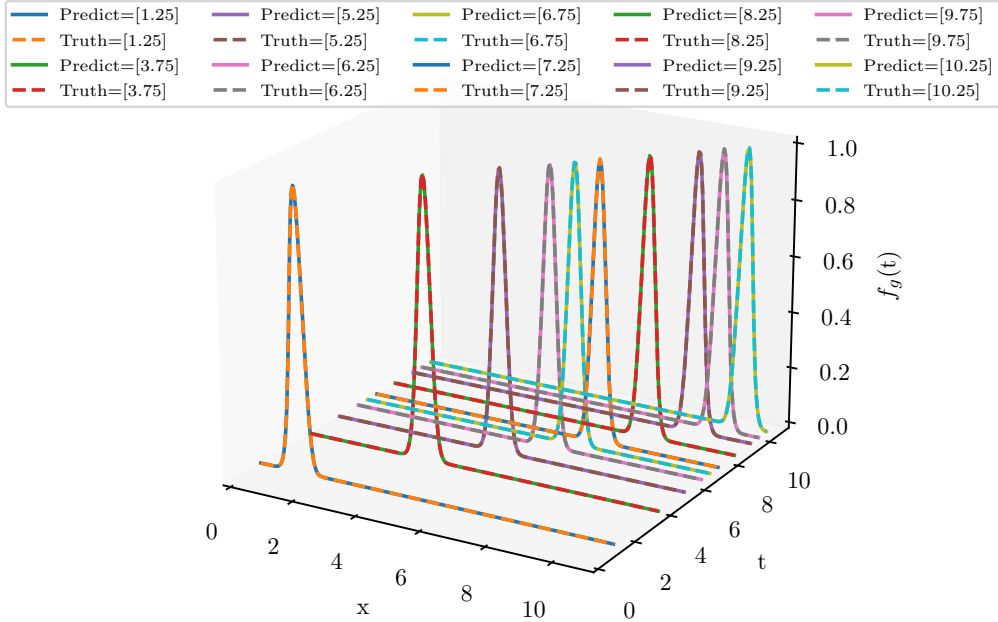


Figure 6: Prediction of NNsPOD-ROM (using 1 NNsPOD mode) for test parameters of the 1D travelling wave, compared with analytical solutions, labelled as Truth.

4.2 2D Isentropic Convective Vortex

We consider the popular higher order methods benchmark case [41, 47], Isentropic Convective Vortex to test our NNsPOD-ROM methodology. The governing equations considered are the 2D Unsteady Euler equations (16), to describe the motion of the inviscid, compressible flow of our benchmark case.

$$\frac{\partial}{\partial t} \begin{bmatrix} \rho \\ \rho u \\ \rho v \\ E \end{bmatrix} + \frac{\partial}{\partial x} \begin{bmatrix} \rho u \\ \rho u^2 + p \\ \rho uv \\ u(E + p) \end{bmatrix} + \frac{\partial}{\partial y} \begin{bmatrix} \rho v \\ \rho uv \\ \rho v^2 + p \\ v(E + p) \end{bmatrix} = 0 \quad (16)$$

where ρ is density, (u, v) are velocity x and y component, p is pressure and E is total energy. The

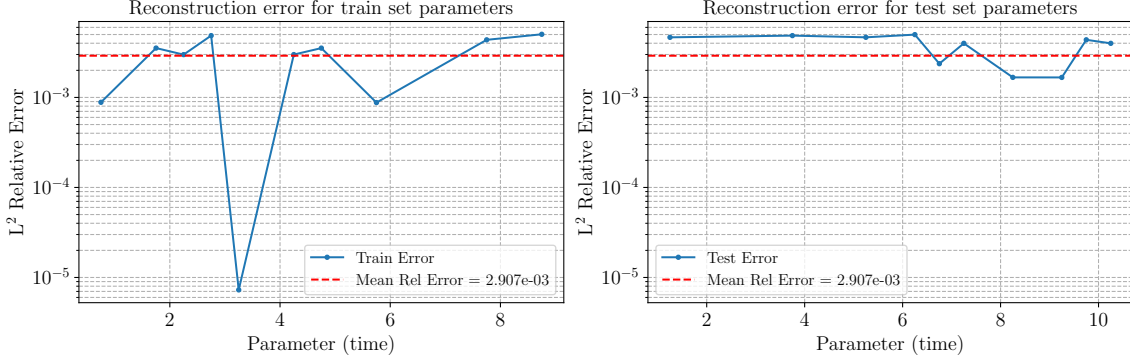


Figure 7: Relative L^2 reconstruction error of predictions by NNsPOD-ROM of the 1D travelling wave, for both train set (left) and test set (right) parameters.

thermodynamic closure is obtained by the total energy equation (17) and in our case we consider constant specific heat ratio, $\gamma = 1.4$ and gas constant, $R_{gas} = 287.15 \text{ J/Kg.K}$.

$$E = \frac{p}{\gamma - 1} + \frac{1}{2}\rho(u^2 + v^2). \quad (17)$$

The initial condition of the freestream flow is given by $\rho_\infty = 1, u_\infty = 0.1, v_\infty = 0, p_\infty = 1$ and the vortex is imposed in the domain by considering the analytical solution as in (18), where vortex strength $b = 0.5$, the radius of the vortex, $r = [(x - x_c)^2 + (y - y_c)^2]^{1/2} = 0.5$ and vortex centre $(x_c, y_c) = (5, 10)$. There are different versions of the vortex problem available in the community [40], we consider the version implemented in the package HyPar 1.0 - Finite Difference Hyperbolic-Parabolic PDE Solver on Cartesian Grids [7] and the results of full-order solutions are obtained using this package.

$$\begin{cases} \rho = \left[1 - \frac{(\gamma-1)b^2}{8\gamma\pi^2} e^{1-r^2}\right]^{\frac{1}{\gamma-1}}, \\ p = \rho^\gamma, \\ u = u_\infty - \frac{b}{2\pi} e^{\frac{1}{2}(1-r^2)} (y - y_c), \\ v = v_\infty + \frac{b}{2\pi} e^{\frac{1}{2}(1-r^2)} (x - x_c). \end{cases} \quad (18)$$

For the approximation of the spatial derivatives of the governing equation, we consider a fifth-order hybrid-compact weighted essentially non-oscillatory (WENO) scheme, which belongs to the class of higher-order accurate numerical methods for hyperbolic PDEs and convection-dominated problems [50]. For time integration, we consider the third-order strong-stability preserving runge-kutta (SSPRK3) method [13].

We consider a domain $\Omega = [0, 40] \times [0, 20]$ discretized into 28800 Cartesian grids, the time interval considered for the simulation is $t \in [0, 62.5]$ with a time step, $\Delta t = 0.625$, yielding snapshots of $N_s = 100$ and leading to the solution manifold definition $\mathcal{M}_h := \{\rho_h(t_i) \in \mathcal{V}_h, i = 1, \dots, 100\}$, consisting of density field snapshots for each time step.

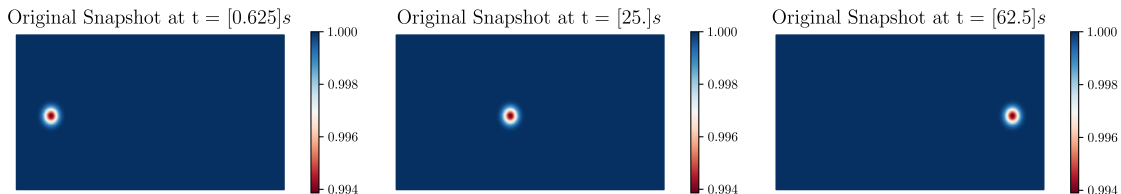


Figure 8: FOM solution of isentropic convective vortex at time, $t \in \{0.625, 25, 62.5\}$ and for pre-processing, the original snapshot at $t = 0.625$ (left) is considered as reference configuration.

For this numerical experiment, we generate a database consisting of 100 snapshots for each time instance, from which we randomly divide 80% of the database into the training set and the remaining 20% into the test set. For the training of neural-network shift augmented transformations of the FOM

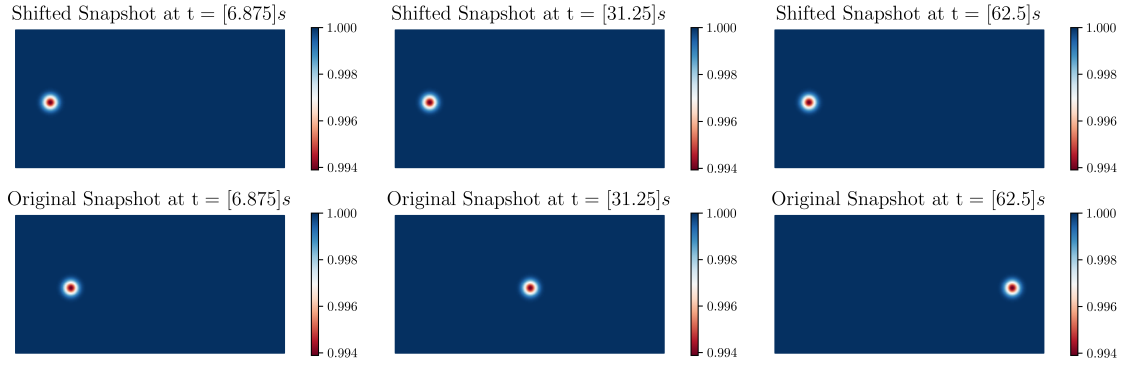


Figure 9: Shifted snapshots (top) of isentropic convective vortex FOM manifold after neural-network shift augmented transformations and the respective original snapshot (bottom) at time, $t \in \{0.625, 25, 62.5\}$ from the training set.

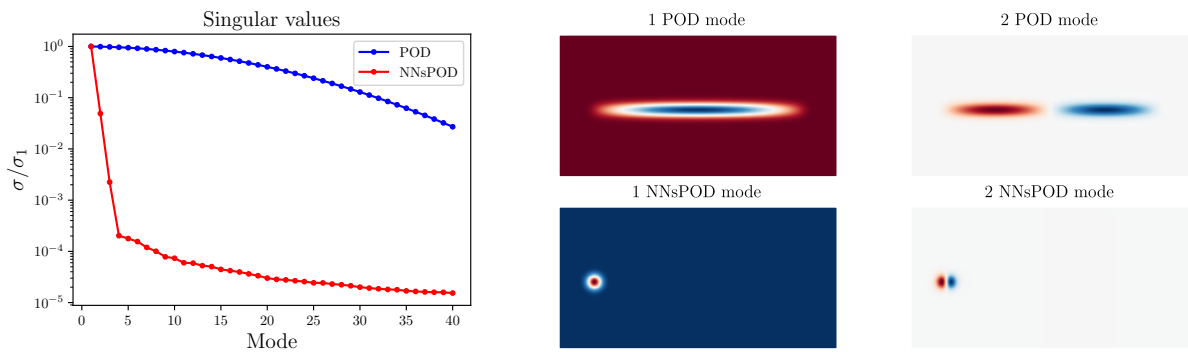


Figure 10: **Left:** Comparison of singular values decay of isentropic convective vortex FOM manifold without transformations, labelled as POD and after the neural-network shifted augmented manifold transformation, labelled as NNsPOD, and **Right:** Showing first two modes of FOM manifold without transformations (first row - POD modes) and after the neural-network shift augmented manifold transformations (second row - NNsPOD modes).

manifold (consisting of the training set), we choose the reference configuration parameter, $t = 0.625$, shown in Figure 8 (left) and learn the shift operator w.r.t the reference configuration. Here, we are shifting only x ordinates, as the vortex is convected in the x-direction. The settings considered for the two neural network architectures for this test case are as shown in Table 3. After the shift-augmented manifold transformation, we obtain shifted snapshots which have been transported to the reference frame as shown in the Figure 9. We perform reduction on this transformed manifold, to obtain sharp singular values decay as shown in Figure 10 (left), compared with singular values obtained without the manifold transformation and also showing the first two modes of FOM manifold without transformations and after the neural -network shift augmented transformations Figure 10(right). It can be depicted that, the NNs-POD captures the vortex structure at the reference frame, while the standard POD fails to capture the vortex structure. Then we obtain the modal coefficients and perform solution manifold approximation, to construct parameter to modal coefficients mapping using the Radial Basis Function (RBF). The predictions for a few unseen parameters of the test set are as shown in the Figure 11, showing the original snapshot (Truth) and the absolute error.

The reconstruction error for the training set parameters and the test set parameters is shown in Figure 12. We plot the predicted snapshots' relative L^2 error for each respective parameter and also show the mean L^2 relative error. The error varies in the same order of magnitude for both train and test set parameters predictions and the error trend increases for the parameters far away from the chosen reference configuration parameter.

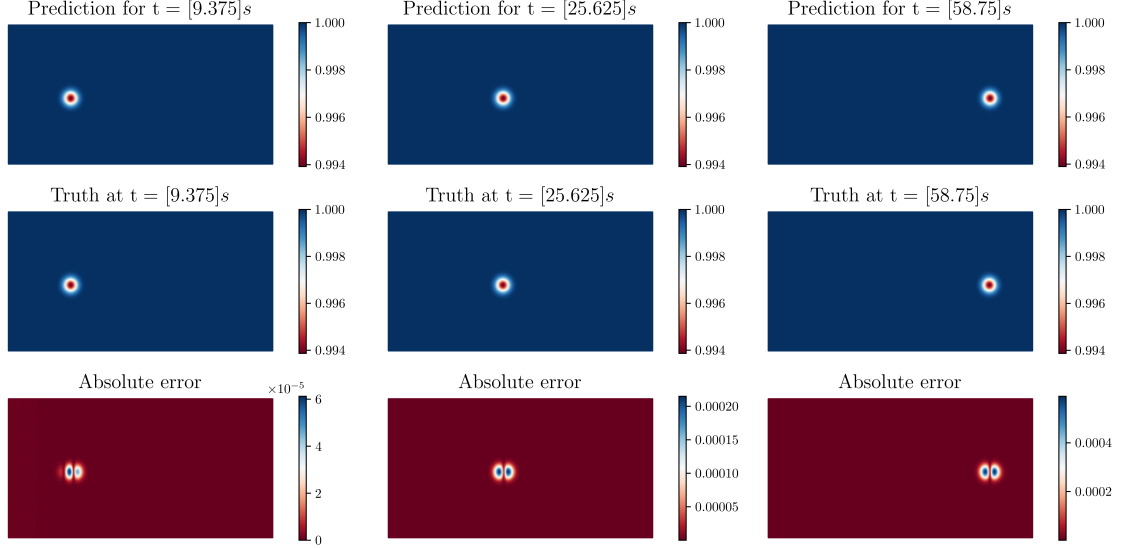


Figure 11: Predictions of snapshots by NNsPOD-ROM of Isentropic Convective Vortex test set parameters, showing for time instances $t = \{9.375, 25.625, 58.75\}$ s.

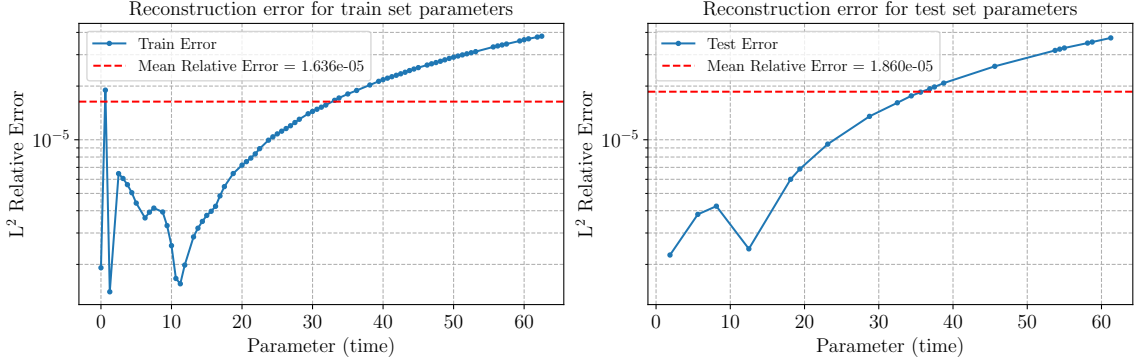


Figure 12: Relative L^2 reconstruction error of predictions by NNsPOD-ROM of Isentropic convective vortex, for both training set (left) and test set (right) parameters.

4.3 2D Two-phase flow

Two-phase flows are governed by the unsteady Navier-Stokes equation (19), with continuity and momentum equation for incompressible fluids, where \mathbf{U} is velocity field, ρ is density, p is pressure and \mathbf{F}_{ST} is the volumetric surface tension.

$$\begin{cases} \nabla \cdot \mathbf{U} = 0, \\ \partial_t(\rho\mathbf{U}) + \nabla \cdot (\rho\mathbf{U} \otimes \mathbf{U}) = -\nabla p + \nabla \cdot [\mu(\nabla\mathbf{U} + \nabla^T\mathbf{U})] + \mathbf{F}_{ST}. \end{cases} \quad (19)$$

For capturing the interface between two-phase flows we consider the one-fluid models approach, which are volume-of-fluids (VOF), level-set (LS) and phase-field (PF) methods. Here, we use the Volume of Fluids (VOF) method, in which the modified volume fraction advection equation (20) is solved simultaneously with continuity and momentum equations. Where $\alpha \in [0, 1]$ is phase fraction which takes values $\alpha = 0$ for gas, $\alpha = 1$ for liquid and at the interface, it ranges between $0 < \alpha < 1$, and \mathbf{U}_r is the relative velocity shown in (21), which is perpendicular to the interface. To solve this advection equation, we use a semi-implicit MULES algorithm.

$$\partial_t\alpha + \nabla \cdot (\alpha\mathbf{U}) + \nabla \cdot [\mathbf{U}_r\alpha(1 - \alpha)] = 0, \quad (20)$$

$$\mathbf{U}_r = C_\alpha |\mathbf{U}| \frac{\nabla \alpha}{|\nabla \alpha|}, \quad \text{with } C_\alpha \in [0, 1]. \quad (21)$$

In the one-fluid model approach, two immiscible fluids are considered as one effective fluid, in which \mathbf{U} acts as the shared velocity of the two fluids $\mathbf{U} = \mathbf{U}_1 = \mathbf{U}_2$. The physical properties of the fluids are averaged over the domain, which leads to constituent relations of ρ and μ weighted values given by:

$$\begin{aligned} \rho &= \alpha_1 \rho_1 + (1 - \alpha_1) \rho_2, \\ \mu &= \alpha_1 \mu_1 + (1 - \alpha_1) \mu_2. \end{aligned} \quad (22)$$

To model the turbulence, we consider $k - \epsilon$ turbulence model based on [23], which is a two-equation linear eddy viscosity turbulence closure model consisting of k - turbulent energy and ϵ - turbulent kinetic energy dissipation rate equations:

$$\begin{cases} \partial_t(\rho k) = \nabla \cdot (\rho D_k \nabla k) + P - \rho \epsilon, \\ \partial_t(\rho \epsilon) = \nabla \cdot (\rho D_\epsilon \nabla \epsilon) + \frac{C_1 \epsilon}{k} (P + C_3 \frac{2}{3} k \nabla \cdot \mathbf{U}) - C_2 \rho \frac{\epsilon^2}{k}. \end{cases} \quad (23)$$

$$\nu_t = C_\mu \frac{k^2}{\epsilon}. \quad (24)$$

where, D_k - effective diffusivity for k , P - turbulent kinetic energy production rate, D_ϵ - effective diffusivity for ϵ , C_1, C_2, C_3 are model coefficients. After obtaining k, ϵ , values, the turbulent viscosity, ν_t is given by (24), here C_μ is the model coefficient for turbulent viscosity. We consider the standard model coefficient values shown in Table 1.

C_μ	C_1	C_2	C_3	σ
0.09	1.44	1.92	0	1

Table 1: Model coefficients of $k - \epsilon$ turbulence model

We consider water ($\rho_1 = 10^3, \nu_1 = 10^{-6}$) and air ($\rho_2 = 1, \nu_2 = 1.48 \times 10^{-5}$) as two fluids for this two-phase flow test case, and consider constant inflow of water into the domain with inlet velocity $\mathbf{U}(x, 0, 0) = (0.5, 0, 0)$. We consider a domain $\Omega = [-0.25, 2] \times [-0.25, 1]$ discretized into 2856 hexahedra cells, the time interval considered for the simulation is $t \in [0, 40]$ with a time step $\Delta t = 0.05$, yielding snapshots of $N_s = 800$ and leading to the solution manifold definition:

$$\mathcal{M}_h := \{\boldsymbol{\alpha}_h(t_i) \in \mathcal{V}_h, i = 1, \dots, 800\}.$$

We construct a database that consists of all these 800 snapshots corresponding for each time instance, here we parameterize time. The full-order solutions of the two-phase flow case are obtained using the interFoam solver [9] of OpenFOAM [49]. The original snapshots at a few time instances are shown in Figure 13 and here, the inlet region at the bottom left and outlet region at the bottom right of the domain can be depicted. We are interested in capturing the interface of two-phase flow and hence, we only consider the region of a domain where the interface evolves, for this reason, we neglect inlet and outlet regions (shown in Figure 14). Once we have the database, we randomly divide 80% of the database as a training set and the rest 20% as a test set. For the training of neural network shift-augmented transformation, we use training set parameters and their corresponding snapshots, and we choose the last snapshot (completely filled configuration) at $t = 40$ s as reference configuration. The settings considered for the two neural network architectures for this test case are as shown in Table 4. InterpNet learns to reconstruct the reference configuration, shown in Figure 14 (bottom right) at $t = 40$. Here, we only shift y coordinates, ShiftNet learns the shift-operator which finds the optimal shift for a given parameter and is used to transport each snapshot to the reference frame as shown in Figure 14.

After neural-network shifted augmented manifold transformations, performing model reduction using SVD, yields singular values as shown in Figure 15. In this case, using neural-network shift augmented transformations is not effective, as we don't achieve significant improvement in accelerating KnW decay and hence, doesn't yield good low-dimensional linear approximations subspace for developing efficient ROM. For this reason, we have a different approach, at first, we learn the shift operator and transform all the snapshots in the training set to reference snapshots via interpolation. For the construction of ROM, the rest of the algorithm remains the same, except for this transformation step.

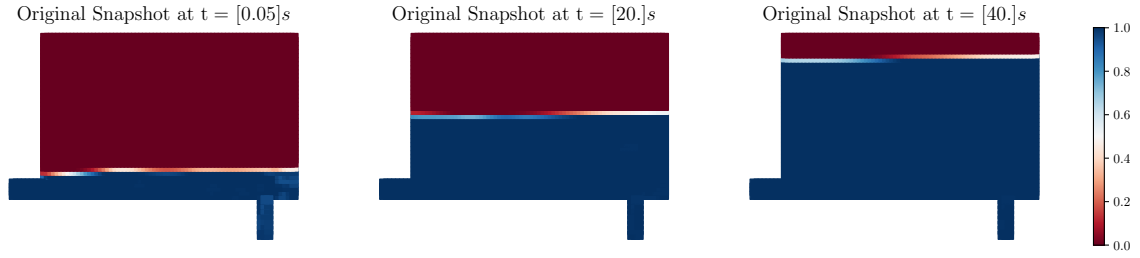


Figure 13: FOM solution of two-phase flow at time, $t \in \{0.05, 20, 40\}$ and for pre-processing of the solution manifold, the original snapshot at $t = 40$ (right figure) is considered as reference configuration.

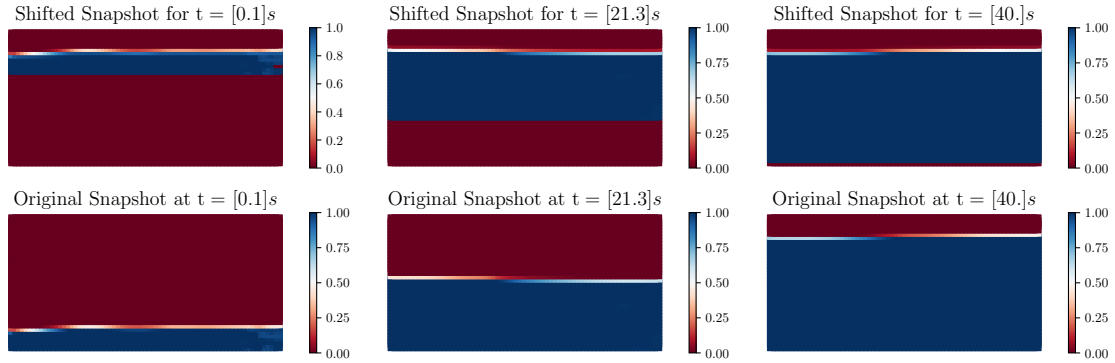


Figure 14: Shifted snapshots (top) of two-phase flow case, after neural-network shift augmented manifold transformations and the respective original snapshot (bottom) at a time, $t = \{0.05, 21.3, 40\}$ from the training set.

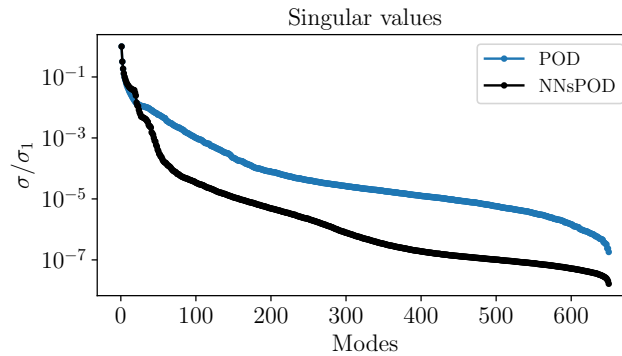


Figure 15: Comparison of singular values decay of two-phase flow FOM manifold without pre-processing, labelled as POD and after the neural-network shifted augmented manifold transformation, labelled as NNsPOD

After transforming all the snapshots to reference snapshot, perform reduction using SVD, the singular values and the first TransformedPOD mode is as shown in the Figure 17. For the construction of ROM, we utilize the first TransformedPOD mode and obtain the coefficient matrix by performing projection. We use RBF to build, parameters to modal coefficient mapping. The predictions for a few test set unseen parameters are shown in Figure 18, with the prediction for three time instances, the respective original snapshot (Truth) and the absolute error. It can be depicted, that the ROM predicts interface locations accurately and with negligible difference in the field values at the interface region. The reconstruction error for both train set and test set parameters is as shown in the Figure 19 and the error varies in the same order of magnitude for both the parameter sets. As the interface evolves over the time interval, the interface region wobbles from the left wall to the right wall of the domains (vice-versa), resulting in this error trend.

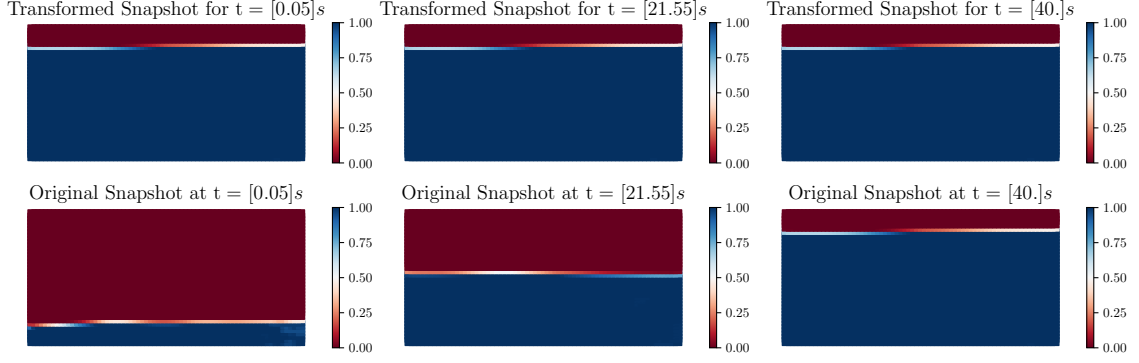


Figure 16: Transformed snapshots (top) of two-phase flow, after transforming all the snapshots to reference snapshot using interpolation to accelerate KnW decay and the respective original snapshot (bottom) at the time, $t = \{0.05, 21.55, 40\}$ from the training set.

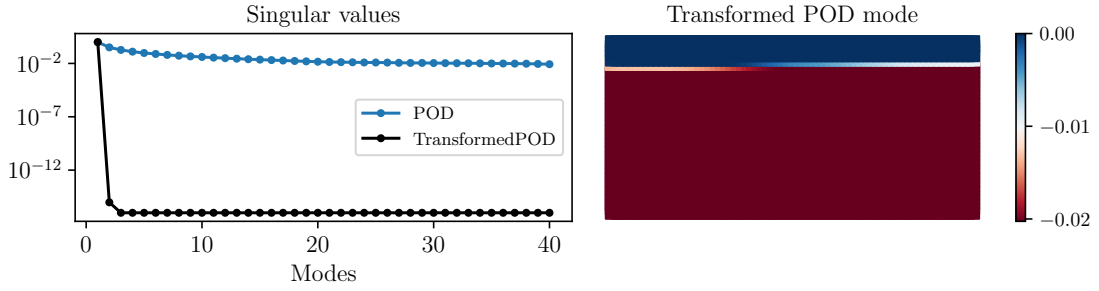


Figure 17: **Left:** Comparison of singular values decay of two-phase flow case FOM manifold without transformations, labelled as POD and after transforming all the snapshots to reference snapshot using interpolation, after learning shift operator, labelled as TransformedPOD, and **Right:** First POD mode obtained after this manifold transformation.

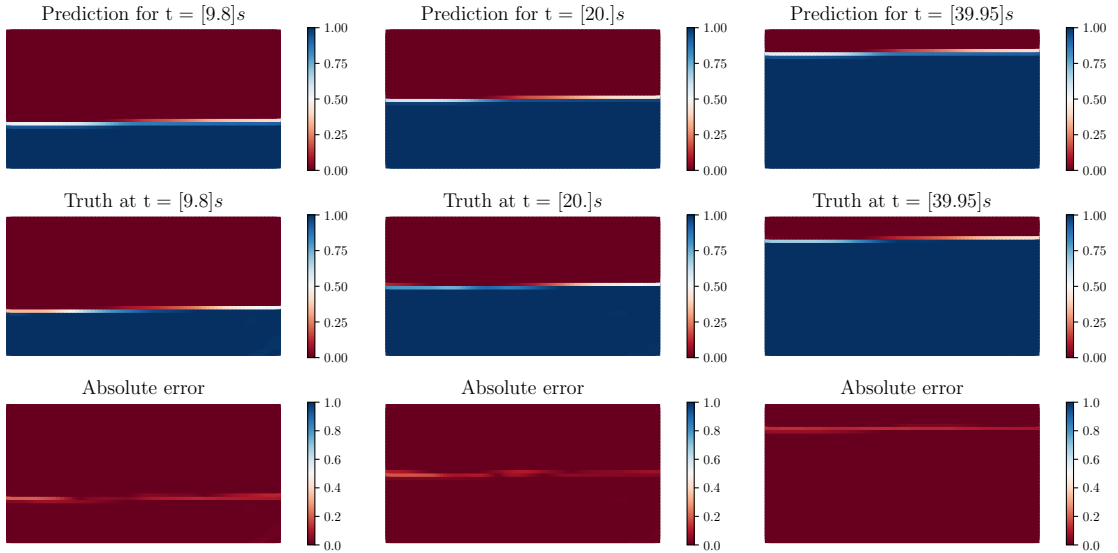


Figure 18: Predictions of snapshots for test set parameters by the resulted TransformedPOD-ROM of the two-phase flow test case, showing predictions for parameters (time) $t = \{9.8, 20, 39.95\}$ s. For the construction of this ROM, we use the transformed linear subspace obtained by transforming all the snapshots in the training set to reference snapshot using interpolation, to accelerate KnW decay. In this case, except for the transformation step, the rest of the proposed algorithm remains the same for the construction of ROM.

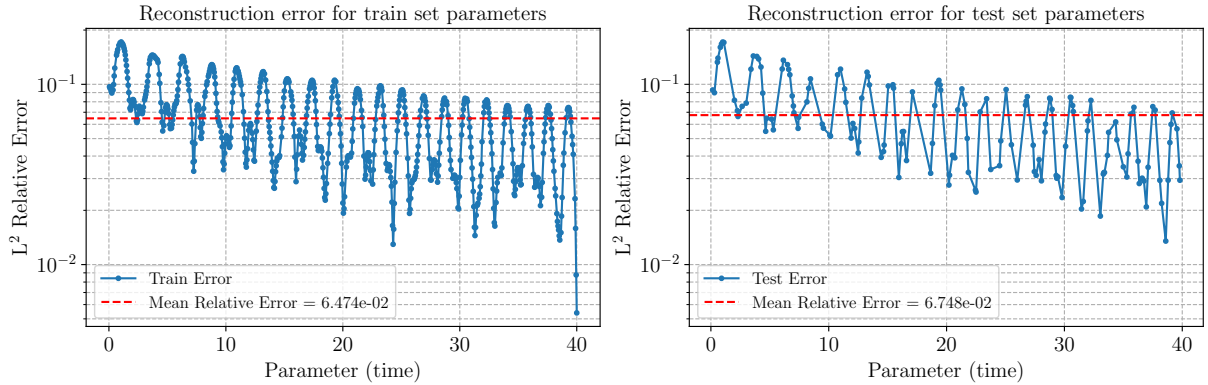


Figure 19: Relative L^2 reconstruction error of predictions by TransformedPOD-ROM of the two-phase flow test case, for both training set (left) and test set (right) parameters.

5 Conclusion

The main focus of this work is the development of a complete NNsPOD-ROM algorithm for advection-dominated problems, comprising of both offline-online stages. To extend the applicability of the automatic shift-detection procedure of the NNsPOD, which introduces neural-network shift augmented manifold transformations (non-linear transformation), without the requirement of the prior knowledge of the underlying equation (physical model) and aiming to derive a better linear approximation of the transformed solution manifold, for the development of efficient ROMs for advection-dominated problems. The main contribution of this work is the construction of ROM on the transformed linear subspace yielded by NNsPOD, the employment of automatic-shift detection in the online stage and thus, resulting in the complete NNsPOD-ROM algorithm. We tested our proposed algorithm on advection-dominated problems of increasing complexity: 1D travelling waves, 2D isentropic convective vortex and 2D two-phase flow test cases. For 1D travelling waves and 2D isentropic convective vortex test cases, the NNsPOD-ROM algorithm results in efficient and accurate ROMs. For the 2D two-phase flow test case, except for the minor adjustment in the transformation step that was required due to the specific configuration of the test case, the rest of the algorithm remains the same and the resulting efficient ROM, predicts accurately the interface location, with negligible small differences in field values at the interface region.

Based on the numerical experiments we performed, the proposed approach results in efficient and accurate ROMs for advection-dominated flow problems. Nevertheless, the application of this approach is limited to specific advection-dominated problems, where the advected features/structure shape should be the same, and this approach is not suitable for advection-diffusion problems. The application of this approach can be extended to developing ROM for particle tracking, for which different neural-network architectures like Long Short-Term Memory (LSTM) or Transformers (well suited for timer series data) can be employed to learn the optimal shift-operator, we postpone this for our future work.

Acknowledgements

We acknowledge the PhD grant supported by industrial partner Danieli & C. S.p.A. and Programma Operativo Nazionale Ricerca e Innovazione 2014-2020, P.I. Gianluigi Rozza.

Appendix

Scaling of data

Before starting the training of neural-networks, we scale the data ranging between the interval $[0,1]$ to improve the prediction accuracy of neural-networks. We use Min-Max scaling for the scaling of training data between the interval $[0, 1]$. The Min-Max scaling for the given matrix U is:

$$U_{ij}^{\text{scaled}} = \frac{U_{ij} - \min_{j=1, \dots, N_s} (U_{ij})}{\max_{j=1, \dots, N_s} (U_{ij}) - \min_{j=1, \dots, N_s} (U_{ij})}, \quad (25)$$

where $i = 1, 2, \dots, n$, number of cells or grid points. The minimum and maximum values are stored and are used to rescale the predicted results back to the original scale.

Neural networks' Architecture

In our numerical experiments, we use Artificial Neural Networks to employ both InterpNet and ShiftNet. The neural network architecture and hyper-parameters considered for each test case are reported here:

Neural network parameters	InterpNet	ShiftNet
Layers	[10, 10]	—
Activation function	SoftPlus	LeakyReLU
Learning rate	0.03	0.0023
Accuracy threshold	10^{-6}	10^{-2}
Optimizer	Adam	Adam

Table 2: 1D Travelling wave test case.

Neural network parameters	InterpNet	ShiftNet
Layers	[40, 40]	[10, 4]
Activation function	Sigmoid	LeakyReLU
Learning rate	0.0023	0.03
Accuracy threshold	1.5×10^{-6}	0.0024
Optimizer	Adam	Adam

Table 3: 2D Isentropic Convective Vortex test case.

Neural network parameters	InterpNet	ShiftNet
Layers	[30, 30]	[10, 4]
Activation function	LeakyReLU	LeakyReLU
Learning rate	0.0023	0.03
Accuracy threshold	5×10^{-7}	0.0005
Optimizer	Adam	Adam

Table 4: 2D Two-phase flow test case.

References

- [1] J. Barnett and C. Farhat. Quadratic approximation manifold for mitigating the Kolmogorov barrier in nonlinear projection-based model order reduction. *Journal of Computational Physics*, 464:111348, Sept. 2022. ISSN 0021-9991. doi: 10.1016/j.jcp.2022.111348. URL <http://dx.doi.org/10.1016/j.jcp.2022.111348>.
- [2] J. Bruna, B. Peherstorfer, and E. Vanden-Eijnden. Neural Galerkin schemes with active learning for high-dimensional evolution equations. *Journal of Computational Physics*, 496:112588, Jan. 2024. ISSN 0021-9991. doi: 10.1016/j.jcp.2023.112588. URL <http://dx.doi.org/10.1016/j.jcp.2023.112588>.
- [3] S. Burela, P. Krahn, and J. Reiss. Parametric model order reduction for a wildland fire model via the shifted pod based deep learning method. *arXiv preprint*, April 2023. doi: 10.48550/arxiv.2304.14872. URL <https://doi.org/10.48550/arxiv.2304.14872>.
- [4] N. Cagniard, R. Crisovan, Y. Maday, and R. Abgrall. Model Order Reduction for Hyperbolic Problems: a new framework. *HAL archive*, 2017. URL <https://hal.science/hal-01583224>.
- [5] F. Chinesta, A. Huerta, G. Rozza, and K. Willcox. Model reduction methods. *Encyclopedia of Computational Mechanics Second Edition*, page 1–36, Dec. 2017. doi: 10.1002/9781119176817.ecm2110. URL <http://dx.doi.org/10.1002/9781119176817.ecm2110>.
- [6] R. Crisovan, D. Torlo, R. Abgrall, and S. Tokareva. Model order reduction for parametrized nonlinear hyperbolic problems as an application to uncertainty quantification. *Journal of Computational and Applied Mathematics*, 348:466–489, March 2019. ISSN 0377-0427. doi: 10.1016/j.cam.2018.09.018. URL <http://dx.doi.org/10.1016/j.cam.2018.09.018>.
- [7] G. Debojyoti, L. John, and Y. Kim. HyPar 1.0 - Finite-Difference Hyperbolic-Parabolic PDE Solver on Cartesian Grids. <https://github.com/debog/hypar>. URL <https://hypar.github.io/index.html>.
- [8] N. Demo, M. Tezzele, and G. Rozza. EZyRB: Easy Reduced Basis method. ”<https://github.com/mathLab/EZyRB>”, April 2018. ISSN 2475-9066. URL <http://dx.doi.org/10.21105/joss.00661>.
- [9] S. S. Deshpande, L. Anumolu, and M. F. Trujillo. Evaluating the performance of the two-phase flow solver interFoam. *Computational Science & Discovery*, 5(1):014016, Nov. 2012. ISSN 1749-4699. doi: 10.1088/1749-4699/5/1/014016. URL <http://dx.doi.org/10.1088/1749-4699/5/1/014016>.
- [10] C. Eckart and G. Young. The approximation of one matrix by another of lower rank. *Psychometrika*, 1(3):211–218, Sept. 1936. ISSN 1860-0980. doi: 10.1007/bf02288367. URL <http://dx.doi.org/10.1007/BF02288367>.
- [11] S. Fresca, L. Dede’, and A. Manzoni. A Comprehensive Deep Learning-Based Approach to Reduced Order Modeling of Nonlinear Time-Dependent Parametrized PDEs. *Journal of Scientific Computing*, 87(2), April 2021. ISSN 1573-7691. doi: 10.1007/s10915-021-01462-7. URL <http://dx.doi.org/10.1007/s10915-021-01462-7>.
- [12] R. Geelen, S. Wright, and K. Willcox. Operator inference for non-intrusive model reduction with quadratic manifolds. *Computer Methods in Applied Mechanics and Engineering*, 403:115717, Jan. 2023. ISSN 0045-7825. doi: 10.1016/j.cma.2022.115717. URL <http://dx.doi.org/10.1016/j.cma.2022.115717>.
- [13] S. Gottlieb, C.-W. Shu, and E. Tadmor. Strong Stability-Preserving High-Order Time Discretization Methods. *SIAM Review*, 43(1):89–112, Jan. 2001. ISSN 1095-7200. doi: 10.1137/s003614450036757x. URL <http://dx.doi.org/10.1137/S003614450036757X>.
- [14] B. Haasdonk and M. Ohlberger. Adaptive basis enrichment for the reduced basis method applied to finite volume schemes. In *Proceedings of the 5th International Symposium on Finite Volumes for Complex Applications*, pages 471–478, 2008.
- [15] D. Hartman and L. K. Mestha. A deep learning framework for model reduction of dynamical systems. In *2017 IEEE Conference on Control Technology and Applications (CCTA)*. IEEE, Aug. 2017. doi: 10.1109/ccta.2017.8062736. URL <http://dx.doi.org/10.1109/CCTA.2017.8062736>.

- [16] J. S. Hesthaven, G. Rozza, and B. Stamm. *Certified Reduced Basis Methods for Parametrized Partial Differential Equations*. Springer International Publishing, 2016. ISBN 9783319224701. doi: 10.1007/978-3-319-22470-1. URL <http://dx.doi.org/10.1007/978-3-319-22470-1>.
- [17] C. Hoang, K. Chowdhary, K. Lee, and J. Ray. Projection-based model reduction of dynamical systems using space–time subspace and machine learning. *Computer Methods in Applied Mechanics and Engineering*, 389:114341, Feb. 2022. ISSN 0045-7825. doi: 10.1016/j.cma.2021.114341. URL <http://dx.doi.org/10.1016/j.cma.2021.114341>.
- [18] A. Iollo and D. Lombardi. Advection modes by optimal mass transfer. *Physical Review E*, 89(2), Feb. 2014. ISSN 1550-2376. doi: 10.1103/physreve.89.022923. URL <http://dx.doi.org/10.1103/PhysRevE.89.022923>.
- [19] S. Jain, P. Tiso, J. B. Rutzmoser, and D. J. Rixen. A quadratic manifold for model order reduction of nonlinear structural dynamics. *Computers & Structures*, 188:80–94, Aug. 2017. ISSN 0045-7949. doi: 10.1016/j.compstruc.2017.04.005. URL <http://dx.doi.org/10.1016/j.compstruc.2017.04.005>.
- [20] K. Kashima. Nonlinear model reduction by deep autoencoder of noise response data. In *2016 IEEE 55th Conference on Decision and Control (CDC)*. IEEE, Dec. 2016. doi: 10.1109/cdc.2016.7799153. URL <http://dx.doi.org/10.1109/CDC.2016.7799153>.
- [21] Y. Kim, Y. Choi, D. Widemann, and T. Zohdi. A fast and accurate physics-informed neural network reduced order model with shallow masked autoencoder. *Journal of Computational Physics*, 451:110841, Feb. 2022. ISSN 0021-9991. doi: 10.1016/j.jcp.2021.110841. URL <http://dx.doi.org/10.1016/j.jcp.2021.110841>.
- [22] A. Kovárnová, P. Kraňh, J. Reiss, and M. Isoz. Shifted Proper Orthogonal Decomposition and Artificial Neural Networks for Time-Continuous Reduced Order Models of Transport-Dominated Systems. In *Topical Problems of Fluid Mechanics 2022*, TPFM. Institute of Thermomechanics of the Czech Academy of Sciences, 2022. doi: 10.14311/tpfm.2022.016. URL <http://dx.doi.org/10.14311/TPFM.2022.016>.
- [23] B. Launder and D. Spalding. The numerical computation of turbulent flows. *Computer Methods in Applied Mechanics and Engineering*, 3(2):269–289, Mar. 1974. ISSN 0045-7825. doi: 10.1016/0045-7825(74)90029-2. URL [http://dx.doi.org/10.1016/0045-7825\(74\)90029-2](http://dx.doi.org/10.1016/0045-7825(74)90029-2).
- [24] K. Lee and K. T. Carlberg. Model reduction of dynamical systems on nonlinear manifolds using deep convolutional autoencoders. *Journal of Computational Physics*, 404:108973, March 2020. ISSN 0021-9991. doi: 10.1016/j.jcp.2019.108973. URL <http://dx.doi.org/10.1016/j.jcp.2019.108973>.
- [25] T. Long, R. Barnett, R. Jefferson-Loveday, G. Stabile, and M. Icardi. A novel reduced-order model for advection-dominated problems based on Radon-Cumulative-Distribution Transform. *arXiv preprint arXiv:2304.14883*, 2023. URL <https://arxiv.org/abs/2304.14883>.
- [26] R. Mojjani and M. Balajewicz. Lagrangian basis method for dimensionality reduction of convection dominated nonlinear flows. *ArXiv*, abs/1701.04343, 2017. URL <https://api.semanticscholar.org/CorpusID:119505364>.
- [27] R. Mojjani and M. Balajewicz. Arbitrary Lagrangian Eulerian framework for efficient projection-based reduction of convection dominated nonlinear flows. In *APS Division of Fluid Dynamics Meeting Abstracts*, pages M1–008, 2017.
- [28] M. Nonino, F. Ballarin, G. Rozza, and Y. Maday. A reduced basis method by means of transport maps for a fluid–structure interaction problem with slowly decaying kolmogorov n -width. *Advances in Computational Science and Engineering*, 1(1):36–58, 2023. ISSN 2837-1739. doi: 10.3934/acse.2023002. URL <http://dx.doi.org/10.3934/acse.2023002>.
- [29] M. Ohlberger and S. Rave. Nonlinear reduced basis approximation of parameterized evolution equations via the method of freezing. *Comptes Rendus. Mathématique*, 351(23–24):901–906, Nov. 2013. ISSN 1778-3569. doi: 10.1016/j.crma.2013.10.028. URL <http://dx.doi.org/10.1016/j.crma.2013.10.028>.

- [30] D. Papapicco, N. Demo, M. Girfoglio, G. Stabile, and G. Rozza. The Neural Network shifted-proper orthogonal decomposition: A machine learning approach for non-linear reduction of hyperbolic equations. *Computer Methods in Applied Mechanics and Engineering*, 392:114687, March 2022. ISSN 0045-7825. doi: 10.1016/j.cma.2022.114687. URL <http://dx.doi.org/10.1016/j.cma.2022.114687>.
- [31] A. Paszke, S. Gross, S. Chintala, G. Chanan, E. Yang, Z. DeVito, Z. Lin, A. Desmaison, L. Antiga, and A. Lerer. Automatic differentiation in PyTorch. In *NIPS Workshop on Automatic differentiation*, 2017.
- [32] B. Peherstorfer. Model Reduction for Transport-Dominated Problems via Online Adaptive Bases and Adaptive Sampling. *SIAM Journal on Scientific Computing*, 42(5):A2803–A2836, Jan. 2020. ISSN 1095-7197. doi: 10.1137/19m1257275. URL <http://dx.doi.org/10.1137/19M1257275>.
- [33] B. Peherstorfer. Breaking the Kolmogorov Barrier with Nonlinear Model Reduction. *Notices of the American Mathematical Society*, 69(05):1, May 2022. ISSN 1088-9477. doi: 10.1090/noti2475. URL <http://dx.doi.org/10.1090/noti2475>.
- [34] B. Peherstorfer and K. Willcox. Online Adaptive Model Reduction for Nonlinear Systems via Low-Rank Updates. *SIAM Journal on Scientific Computing*, 37(4):A2123–A2150, Jan. 2015. ISSN 1095-7197. doi: 10.1137/140989169. URL <http://dx.doi.org/10.1137/140989169>.
- [35] A. Quarteroni, A. Manzoni, and F. Negri. *Reduced Basis Methods for Partial Differential Equations*. Springer International Publishing, 2016. ISBN 9783319154312. doi: 10.1007/978-3-319-15431-2. URL <http://dx.doi.org/10.1007/978-3-319-15431-2>.
- [36] J. Reiss, P. Schulze, J. Sesterhenn, and V. Mehrmann. The Shifted Proper Orthogonal Decomposition: A Mode Decomposition for Multiple Transport Phenomena. *SIAM Journal on Scientific Computing*, 40(3):A1322–A1344, Jan. 2018. ISSN 1095-7197. doi: 10.1137/17m1140571. URL <http://dx.doi.org/10.1137/17M1140571>.
- [37] D. Rim, S. Moe, and R. J. LeVeque. Transport Reversal for Model Reduction of Hyperbolic Partial Differential Equations. *SIAM/ASA Journal on Uncertainty Quantification*, 6(1):118–150, Jan. 2018. ISSN 2166-2525. doi: 10.1137/17m1113679. URL <http://dx.doi.org/10.1137/17M1113679>.
- [38] F. Romor, G. Stabile, and G. Rozza. Non-linear Manifold Reduced-Order Models with Convolutional Autoencoders and Reduced Over-Collocation Method. *Journal of Scientific Computing*, 94(3), Feb. 2023. ISSN 1573-7691. doi: 10.1007/s10915-023-02128-2. URL <http://dx.doi.org/10.1007/s10915-023-02128-2>.
- [39] G. Rozza, G. Stabile, and F. Ballarin. *Advanced Reduced Order Methods and Applications in Computational Fluid Dynamics*. Society for Industrial and Applied Mathematics, Jan 2022. ISBN 9781611977257. doi: 10.1137/1.9781611977257. URL <http://dx.doi.org/10.1137/1.9781611977257>.
- [40] C.-W. Shu. *Essentially non-oscillatory and weighted essentially non-oscillatory schemes for hyperbolic conservation laws*, page 325–432. Springer Berlin Heidelberg, 1998. ISBN 9783540498049. doi: 10.1007/bfb0096355. URL <http://dx.doi.org/10.1007/BFb0096355>.
- [41] S. C. Spiegel, H. Huynh, and J. R. DeBonis. A survey of the isentropic euler vortex problem using high-order methods. In *22nd AIAA Computational Fluid Dynamics Conference*. American Institute of Aeronautics and Astronautics, June 2015. doi: 10.2514/6.2015-2444. URL <http://dx.doi.org/10.2514/6.2015-2444>.
- [42] G. Stabile and G. Rozza. Finite volume pod-galerkin stabilised reduced order methods for the parametrised incompressible navier–stokes equations. *Computers & Fluids*, 173:273–284, Sept. 2018. ISSN 0045-7930. doi: 10.1016/j.compfluid.2018.01.035. URL <http://dx.doi.org/10.1016/j.compfluid.2018.01.035>.
- [43] G. Stabile, F. Ballarin, G. Zuccarino, and G. Rozza. A reduced order variational multiscale approach for turbulent flows. *Advances in Computational Mathematics*, 45(5–6):2349–2368, June 2019. ISSN 1572-9044. doi: 10.1007/s10444-019-09712-x. URL <http://dx.doi.org/10.1007/s10444-019-09712-x>.

- [44] G. W. Stewart. On the Early History of the Singular Value Decomposition. *SIAM Review*, 35(4): 551–566, Dec 1993. ISSN 1095-7200. doi: 10.1137/1035134. URL <http://dx.doi.org/10.1137/1035134>.
- [45] T. Taddei. A Registration Method for Model Order Reduction: Data Compression and Geometry Reduction. *SIAM Journal on Scientific Computing*, 42(2):A997–A1027, Jan. 2020. ISSN 1095-7197. doi: 10.1137/19m1271270. URL <http://dx.doi.org/10.1137/19M1271270>.
- [46] D. Torlo. Model Reduction for Advection Dominated Hyperbolic Problems in an ALE Framework: Offline and Online Phases. *arXiv preprint*, March 2020. doi: 10.48550/arxiv.2003.13735. URL <https://arxiv.org/abs/2003.13735>.
- [47] Z. Wang, K. Fidkowski, R. Abgrall, F. Bassi, D. Caraeni, A. Cary, H. Deconinck, R. Hartmann, K. Hillewaert, H. Huynh, N. Kroll, G. May, P. Persson, B. van Leer, and M. Visbal. High-order cfd methods: current status and perspective. *International Journal for Numerical Methods in Fluids*, 72(8):811–845, Jan. 2013. ISSN 1097-0363. doi: 10.1002/flid.3767. URL <http://dx.doi.org/10.1002/flid.3767>.
- [48] K. Washabaugh, D. Amsallem, M. Zahr, and C. Farhat. Nonlinear Model Reduction for CFD Problems Using Local Reduced-Order Bases. In *42nd AIAA Fluid Dynamics Conference and Exhibit*. American Institute of Aeronautics and Astronautics, June 2012. doi: 10.2514/6.2012-2686. URL <http://dx.doi.org/10.2514/6.2012-2686>.
- [49] H. G. Weller, G. Tabor, H. Jasak, and C. Fureby. A tensorial approach to computational continuum mechanics using object-oriented techniques. *Computers in Physics*, 12(6):620–631, Nov. 1998. ISSN 0894-1866. doi: 10.1063/1.168744. URL <http://dx.doi.org/10.1063/1.168744>.
- [50] Y.-T. Zhang and C.-W. Shu. ENO and WENO Schemes . In *Handbook of Numerical Methods for Hyperbolic Problems - Basic and Fundamental Issues*, page 103–122. Elsevier, 2016. doi: 10.1016/bs.hna.2016.09.009. URL <http://dx.doi.org/10.1016/bs.hna.2016.09.009>.